



A Tale of Three: Magnetic Fields along the Orion Integral-shaped Filament as Revealed by the JCMT BISTRO Survey

Downloaded from: <https://research.chalmers.se>, 2025-06-09 14:40 UTC

Citation for the original published paper (version of record):

Wu, J., Qiu, K., Poidevin, F. et al (2024). A Tale of Three: Magnetic Fields along the Orion Integral-shaped Filament as Revealed by the JCMT BISTRO Survey. *Astrophysical Journal Letters*, 977(2).
<http://dx.doi.org/10.3847/2041-8213/ad93d2>

N.B. When citing this work, cite the original published paper.



A Tale of Three: Magnetic Fields along the Orion Integral-shaped Filament as Revealed by the JCMT BISTRO Survey

Jintai Wu^{1,2} , Keping Qiu^{1,2} , Frédéric Poidevin^{3,4} , Pierre Bastien⁵ , Junhao Liu⁶ , Tao-Chung Ching⁷ , Tyler L. Bourke^{8,9} , Derek Ward-Thompson¹⁰ , Kate Pattle¹¹ , Doug Johnstone^{12,13} , Patrick M. Koch¹⁴ , Doris Arzoumanian¹⁵ , Chang Won Lee^{16,17} , Lapo Fanciullo¹⁸ , Takashi Onaka¹⁹ , Jihye Hwang¹⁶ , Valentin J. M. Le Gouellec^{20,21} , Archana Soam²² , Motohide Tamura^{19,23,24} , Mehrnoosh Tahani²⁵ , Chakali Eswaraiah²⁶ , Hua-Bai Li²⁷ , David Berry²⁸ , Ray S. Furuya²⁹ , Simon Coudé^{30,31} , Woojin Kwon^{32,33,34} , Sheng-Jun Lin¹⁴ , Jia-Wei Wang¹⁴ , Tetsuo Hasegawa²³ , Shih-Ping Lai^{14,35} , Do-Young Byun^{16,17} , Zhiwei Chen³⁶ , Huei-Ru Vivien Chen^{14,35} , Wen Ping Chen³⁷ , Mike Chen¹³ , Jungyeon Cho³⁸ , Youngwoo Choi³⁹ , Yunhee Choi¹⁶ , Minhoo Choi¹⁶ , Antonio Chrysostomou⁸ , Eun Jung Chung¹⁶ , Sophia Dai⁴⁰ , James Di Francesco^{12,13} , Pham Ngoc Diep⁴¹ , Yasuo Doi⁴² , Hao-Yuan Duan⁴³ , Yan Duan⁴⁰ , David Eden⁴⁴ , Jason Fiege⁴⁵ , Laura M. Fissel⁴⁶ , Erica Franzmann⁴⁵ , Per Friberg²⁸ , Rachel Friesen⁴⁷ , Gary Fuller⁹ , Tim Gledhill⁴⁸ , Sarah Graves²⁸ , Jane Greaves⁴⁹ , Matt Griffin⁴⁹ , Qilao Gu⁵⁰ , Ilseung Han^{16,17} , Saeko Hayashi⁵¹ , Thiem Hoang^{16,17} , Martin Houde⁵² , Tsuyoshi Inoue⁵³ , Shu-ichiro Inutsuka⁵⁴ , Kazunari Iwasaki⁵⁵ , Il-Gyo Jeong^{16,56} , Vera Könyves¹⁰ , Ji-hyun Kang¹⁶ , Miju Kang¹⁶ , Janik Karoly¹¹ , Akimasa Kataoka⁵⁷ , Koji Kawabata^{58,59,60} , Shinyoung Kim¹⁶ , Mi-Ryang Kim⁶¹ , Kyoung Hee Kim⁶² , Kee-Tae Kim^{16,17} , Jongsoo Kim^{16,17} , Hyosung Kim³² , Gwanjeong Kim⁶³ , Florian Kirchschlager⁶⁴ , Jason Kirk¹⁰ , Masato I.N. Kobayashi⁶⁵ , Takayoshi Kusune⁶⁶ , Jungmi Kwon¹⁹ , Kevin Lacaille^{67,68} , Chi-Yan Law⁷⁵ , Hyeeseung Lee¹⁴ , Chin-Fei Lee¹⁴ , Sang-Sung Lee^{16,17} , Jeong-Eun Lee⁷¹ , Dalei Li⁷² , Di Li^{73,74} , Guangxing Li⁷⁵ , Sheng-Yuan Liu¹⁴ , Tie Liu⁷⁶ , Hong-Li Liu⁷⁷ , Xing Lu⁵⁰ , A-Ran Lyo¹⁶ , Steve Mairs²⁸ , Masafumi Matsumura⁷⁸ , Brenda Matthews^{12,13} , Gerald Moriarty-Schieven¹² , Tetsuya Nagata⁷⁹ , Fumitaka Nakamura^{57,80} , Hiroyuki Nakanishi⁸¹ , Nguyen Bich Ngoc^{41,82} , Nagayoshi Ohashi¹⁴ , Geumsook Park¹⁶ , Harriet Parsons²⁸ , Nicolas Peretto⁴⁹ , Felix Priestley⁴⁹ , Tae-Soo Pyo^{80,83} , Lei Qian⁷³ , Ramprasad Rao¹⁴ , Jonathan Rawlings¹¹ , Mark Rawlings^{28,84} , Brendan Retter⁴⁹ , John Richer^{85,86} , Andrew Rigby⁴⁹ , Sarah Sadavoy⁴⁶ , Hiro Saito⁸⁷ , Giorgio Savini⁸⁸ , Masumichi Seta⁸⁹ , Ekta Sharma⁷³ , Yoshito Shimajiri⁹⁰ , Hiroko Shinnaga⁸¹ , Ya-Wen Tang¹⁴ , Xindi Tang⁹¹ , Hoang Duc Thuong⁹² , Kohji Tomisaka⁵⁷ , Le Ngoc Tram⁹³ , Yusuke Tsukamoto⁸¹ , Serena Viti⁹⁴ , Hongchi Wang³⁶ , Anthony Whitworth⁴⁹ , Jinjin Xie⁴⁰ , Meng-Zhe Yang³⁵ , Hsi-Wei Yen¹⁴ , Hyunju Yoo³⁸ , Jinghua Yuan⁴⁰ , Hyeong-Sik Yun¹⁶ , Tetsuya Zenko⁷⁹ , Guoyin Zhang⁷³ , Chuan-Peng Zhang^{40,73} , Yapeng Zhang⁹⁵ , Jianjun Zhou⁷² , Lei Zhu⁷³ , Ilse de Looze⁶⁴ , Philippe André⁹⁶ , C. Darren Dowell⁹⁷ , Stewart Eyres⁹⁸ , Sam Falle⁹⁹ , Jean-François Robitaille¹⁰⁰ , and Sven van Loo¹⁰¹

¹ School of Astronomy and Space Science, Nanjing University, 163 Xianlin Avenue, Nanjing 210023, People's Republic of China; kpqiu@nju.edu.cn

² Key Laboratory of Modern Astronomy and Astrophysics (Nanjing University), Ministry of Education, Nanjing 210023, People's Republic of China

³ Instituto de Astrofísica de Canarias, E-38205 La Laguna, Tenerife, Canary Islands, Spain

⁴ Universidad de La Laguna, Dpto. Astrofísica, E-38206 La Laguna, Tenerife, Spain

⁵ Centre de recherche en astrophysique du Québec & département de physique, Université de Montréal, 1375, Avenue Thérese-Lavoie-Roux, Montréal, QC, H2V 0B3, Canada

⁶ Division of ALMA, National Astronomical Observatory of Japan, Mitaka, Tokyo 181-8588, Japan

⁷ National Radio Astronomy Observatory, 1003 Lopezville Road, Socorro, NM 87801, USA

⁸ SKA Observatory, Jodrell Bank, Lower Withington, Macclesfield SK11 9FT, UK

⁹ Jodrell Bank Centre for Astrophysics, School of Physics and Astronomy, University of Manchester, Oxford Road, Manchester, M13 9PL, UK

¹⁰ Jeremiah Horrocks Institute, University of Central Lancashire, Preston PR1 2HE, UK

¹¹ Department of Physics and Astronomy, University College London, Gower Street, WC1E 6BT London, UK

¹² NRC Herzberg Astronomy and Astrophysics, 5071 West Saanich Road, Victoria, BC V9E 2E7, Canada

¹³ Department of Physics and Astronomy, University of Victoria, Victoria, BC V8W 2Y2, Canada

¹⁴ Academia Sinica Institute of Astronomy and Astrophysics, No.1, Sec. 4., Roosevelt Road, Taipei 10617, Taiwan

¹⁵ Division of Science, National Astronomical Observatory of Japan, 2-21-1 Osawa, Mitaka, Tokyo 181-8588, Japan

¹⁶ Korea Astronomy and Space Science Institute, 776 Daedeokdae-ro, Yuseong-gu, Daejeon 34055, Republic of Korea

¹⁷ University of Science and Technology, Korea, 217 Gajeong-ro, Yuseong-gu, Daejeon 34113, Republic of Korea

¹⁸ National Chung Hsing University, 145 Xingda Road, South District, Taichung City 402, Taiwan

¹⁹ Department of Astronomy, Graduate School of Science, The University of Tokyo, 7-3-1 Hongo, Bunkyo-ku, Tokyo 113-0033, Japan

²⁰ NASA Ames Research Center, Space Science and Astrobiology Division, M.S. 245-6, Moffett Field, CA 94035, USA

²¹ NASA Postdoctoral Program Fellow

²² Indian Institute of Astrophysics, II Block, Koramangala, Bengaluru 560034, India

²³ National Astronomical Observatory of Japan, National Institutes of Natural Sciences, Osawa, Mitaka, Tokyo 181-8588, Japan

²⁴ Astrobiology Center, National Institutes of Natural Sciences, 2-21-1 Osawa, Mitaka, Tokyo 181-8588, Japan

²⁵ Banting and KIPAC Fellow: Kavli Institute for Particle Astrophysics and Cosmology (KIPAC), Stanford University, Stanford, CA, USA

²⁶ Indian Institute of Science Education and Research (IISER) Tirupati, Rami Reddy Nagar, Karakambadi Road, Mangalam (P.O.), Tirupati 517 507, India

²⁷ Department of Physics, The Chinese University of Hong Kong, Shatin, N.T., Hong Kong

²⁸ East Asian Observatory, 660 North A'ohoku Place, University Park, Hilo, HI 96720, USA

²⁹ Institute of Liberal Arts and Sciences Tokushima University, Minami Jousanajima-machi 1-1, Tokushima 770-8502, Japan

³⁰ Department of Earth, Environment, and Physics, Worcester State University, Worcester, MA 01602, USA

³¹ Center for Astrophysics | Harvard & Smithsonian, 60 Garden Street, Cambridge, MA 02138, USA

³² Department of Earth Science Education, Seoul National University, 1 Gwanak-ro, Gwanak-gu, Seoul 08826, Republic of Korea

³³ SNU Astronomy Research Center, Seoul National University, 1 Gwanak-ro, Gwanak-gu, Seoul 08826, Republic of Korea

³⁴ The Center for Educational Research, Seoul National University, 1 Gwanak-ro, Gwanak-gu, Seoul 08826, Republic of Korea

- ³⁵ Institute of Astronomy and Department of Physics, National Tsing Hua University, Hsinchu 30013, Taiwan
- ³⁶ Purple Mountain Observatory, Chinese Academy of Sciences, 2 West Beijing Road, 210008 Nanjing, People's Republic of China
- ³⁷ Institute of Astronomy, National Central University, Zhongli 32001, Taiwan
- ³⁸ Department of Astronomy and Space Science, Chungnam National University, 99 Daehak-ro, Yuseong-gu, Daejeon 34134, Republic of Korea
- ³⁹ Department of Physics and Astronomy, Seoul National University, 1 Gwanak-ro, Gwanak-gu, Seoul 08826, Republic of Korea
- ⁴⁰ National Astronomical Observatories, Chinese Academy of Sciences, A20 Datun Road, Chaoyang District, Beijing 100012, People's Republic of China
- ⁴¹ Vietnam National Space Center, Vietnam Academy of Science and Technology, 18 Hoang Quoc Viet, Hanoi, Vietnam
- ⁴² Department of Earth Science and Astronomy, Graduate School of Arts and Sciences, The University of Tokyo, 3-8-1 Komaba, Meguro, Tokyo 153-8902, Japan
- ⁴³ Taipei Astronomical Museum, 111013 No.363, Jihe Road, Shilin District, Taipei, Taiwan, R.O.C
- ⁴⁴ Armagh Observatory and Planetarium, College Hill, Armagh BT61 9DB, UK
- ⁴⁵ Department of Physics and Astronomy, The University of Manitoba, Winnipeg, MB R3T2N2, Canada
- ⁴⁶ Department for Physics, Engineering Physics and Astrophysics, Queen's University, Kingston, ON K7L 3N6, Canada
- ⁴⁷ National Radio Astronomy Observatory, 520 Edgemont Road, Charlottesville, VA 22903, USA
- ⁴⁸ School of Physics, Astronomy & Mathematics, University of Hertfordshire, College Lane, Hatfield, Hertfordshire AL10 9AB, UK
- ⁴⁹ School of Physics and Astronomy, Cardiff University, The Parade, Cardiff, CF24 3AA, UK
- ⁵⁰ Shanghai Astronomical Observatory, Chinese Academy of Sciences, 80 Nandan Road, Shanghai 200030, People's Republic of China
- ⁵¹ Kavli Institute for the Physics and Mathematics of the Universe, The University of Tokyo, 5-1-5 Kashiwanoha, Kashiwa, Chiba, 277-8583, Japan
- ⁵² Department of Physics and Astronomy, The University of Western Ontario, 1151 Richmond Street, London N6A 3K7, Canada
- ⁵³ Department of Physics, Konan University, Okamoto 8-9-1, Higashinada-ku, Kobe 658-8501, Japan
- ⁵⁴ Department of Physics, Graduate School of Science, Nagoya University, Furo-cho, Chikusa-ku, Nagoya 464-8602, Japan
- ⁵⁵ Center for Computational Astrophysics, National Astronomical Observatory of Japan, Mitaka, Tokyo 181-8588, Japan
- ⁵⁶ Department of Astronomy and Atmospheric Sciences, Kyungpook National University, Daegu 41566, Republic of Korea
- ⁵⁷ Division of Theoretical Astronomy, National Astronomical Observatory of Japan, Mitaka, Tokyo 181-8588, Japan
- ⁵⁸ Hiroshima Astrophysical Science Center, Hiroshima University, Kagamiyama 1-3-1, Higashi-Hiroshima, Hiroshima 739-8526, Japan
- ⁵⁹ Department of Physics, Hiroshima University, Kagamiyama 1-3-1, Higashi-Hiroshima, Hiroshima 739-8526, Japan
- ⁶⁰ Core Research for Energetic Universe (CORE-U), Hiroshima University, Kagamiyama 1-3-1, Higashi-Hiroshima, Hiroshima 739-8526, Japan
- ⁶¹ School of Space Research, Kyung Hee University, 1732 Deogyong-daero, Giheung-gu, Yongin-si, Gyeonggi-do 17104, Republic of Korea
- ⁶² Ulsan National Institute of Science and Technology (UNIST), UNIST-gil 50, Eonyang-eup, Ulju-gun, Ulsan 44919, Republic of Korea
- ⁶³ Nobeyama Radio Observatory, National Astronomical Observatory of Japan, National Institutes of Natural Sciences, Nobeyama, Minamimaki, Minamisaka, Nagano 384-1305, Japan
- ⁶⁴ Sterrenkundig Observatorium, Ghent University, Krijgslaan 281-S9, 9000 Gent, Belgium
- ⁶⁵ Physikalisches Institut, University of Cologne, Zùlpicher Str. 77, D-50937 Köln, Germany
- ⁶⁶ Astronomical Institute, Graduate School of Science, Tohoku University, Aoba-ku, Sendai, Miyagi 980-8578, Japan
- ⁶⁷ Department of Physics and Astronomy, McMaster University, Hamilton, ON L8S 4M1, Canada
- ⁶⁸ Department of Physics and Atmospheric Science, Dalhousie University, Halifax B3H 4R2, Canada
- ⁶⁹ Department of Space, Earth & Environment, Chalmers University of Technology, SE-412 96 Gothenburg, Sweden
- ⁷⁰ Ulsan National Institute of Science and Technology (UNIST), 50 UNIST-gil, Ulsan 44919, Republic of Korea
- ⁷¹ Astronomy Program, Department of Physics and Astronomy, Seoul National University, 1 Gwanak-ro, Gwanak-gu, Seoul 08826, Republic of Korea
- ⁷² Xinjiang Astronomical Observatory, Chinese Academy of Sciences, 150 Science 1-Street, Urumqi 830011, Xinjiang, People's Republic of China
- ⁷³ CAS Key Laboratory of FAST, National Astronomical Observatories, Chinese Academy of Sciences, People's Republic of China
- ⁷⁴ University of Chinese Academy of Sciences, Beijing 100049, People's Republic of China
- ⁷⁵ South-Western Institute for Astronomy Research, Yunnan University, Kunming 650500, People's Republic of China
- ⁷⁶ Key Laboratory for Research in Galaxies and Cosmology, Shanghai Astronomical Observatory, Chinese Academy of Sciences, 80 Nandan Road, Shanghai 200030, People's Republic of China
- ⁷⁷ Department of Astronomy, Yunnan University, Kunming, 650091, People's Republic of China
- ⁷⁸ Faculty of Education & Center for Educational Development and Support, Kagawa University, Saiwai-cho 1-1, Takamatsu, Kagawa, 760-8522, Japan
- ⁷⁹ Department of Astronomy, Graduate School of Science, Kyoto University, Sakyo-ku, Kyoto 606-8502, Japan
- ⁸⁰ SOKENDAI (The Graduate University for Advanced Studies), Hayama, Kanagawa 240-0193, Japan
- ⁸¹ Department of Physics and Astronomy, Graduate School of Science and Engineering, Kagoshima University, 1-21-35 Korimoto, Kagoshima, Kagoshima 890-0065, Japan
- ⁸² Graduate University of Science and Technology, Vietnam Academy of Science and Technology, 18 Hoang Quoc Viet, Cau Giay, Hanoi, Vietnam
- ⁸³ Subaru Telescope, National Astronomical Observatory of Japan, 650 North A'ohokū Place, Hilo, HI 96720, USA
- ⁸⁴ Gemini Observatory/NSF NOIRLab, 670 N. A'ohokū Place, Hilo, HI 96720, USA
- ⁸⁵ Astrophysics Group, Cavendish Laboratory, J. J. Thomson Avenue, Cambridge CB3 0HE, UK
- ⁸⁶ Kavli Institute for Cosmology, Institute of Astronomy, University of Cambridge, Madingley Road, Cambridge, CB3 0HA, UK
- ⁸⁷ Faculty of Pure and Applied Sciences, University of Tsukuba, 1-1-1 Tennodai, Tsukuba, Ibaraki 305-8577, Japan
- ⁸⁸ OSL, Physics & Astronomy Department, University College London, WC1E 6BT London, UK
- ⁸⁹ Department of Physics, School of Science and Technology, Kwansei Gakuin University, 2-1 Gakuen, Sanda, Hyogo 669-1337, Japan
- ⁹⁰ Kyushu Kyoritsu University, 1-8, Jiyugaoka, Yahatanishi-ku, Kitakyushu-shi, Fukuoka 807-8585, Japan
- ⁹¹ Xinjiang Astronomical Observatory, Chinese Academy of Sciences, 830011 Urumqi, People's Republic of China
- ⁹² School of Physics and Astronomy, University of Minnesota, Minneapolis, MN 55455, USA
- ⁹³ Leiden Observatory, Leiden University, PO Box 9513, 2300 RA Leiden, The Netherlands
- ⁹⁴ Physics & Astronomy Department, University College London, WC1E 6BT London, UK
- ⁹⁵ Department of Astronomy, Beijing Normal University, Beijing 100875, People's Republic of China
- ⁹⁶ Laboratoire AIM CEA/DSM-CNRS-Université Paris Diderot, IRFU/Service d'Astrophysique, CEA Saclay, F-91191 Gif-sur-Yvette, France
- ⁹⁷ Jet Propulsion Laboratory, M/S 169-506, 4800 Oak Grove Drive, Pasadena, CA 91109, USA
- ⁹⁸ University of South Wales, Pontypridd, CF37 1DL, UK
- ⁹⁹ Department of Applied Mathematics, University of Leeds, Woodhouse Lane, Leeds LS2 9JT, UK
- ¹⁰⁰ Univ. Grenoble Alpes, CNRS, IPAG, 38000 Grenoble, France
- ¹⁰¹ School of Physics and Astronomy, University of Leeds, Woodhouse Lane, Leeds LS2 9JT, UK

Received 2024 September 03; revised 2024 November 13; accepted 2024 November 17; published 2024 December 11



Original content from this work may be used under the terms of the [Creative Commons Attribution 4.0 licence](https://creativecommons.org/licenses/by/4.0/). Any further distribution of this work must maintain attribution to the author(s) and the title of the work, journal citation and DOI.

Abstract

As part of the *B*-fields In Star-forming Region Observations survey, we present James Clerk Maxwell Telescope (JCMT) 850 μm polarimetric observations toward the Orion integral-shaped filament (ISF) that covers three portions known as OMC-1, OMC-2, and OMC-3. The magnetic field threading the ISF seen in the JCMT POL-2 map appears as a tale of three: pinched for OMC-1, twisted for OMC-2, and nearly uniform for OMC-3. A multiscale analysis shows that the magnetic field structure in OMC-3 is very consistent at all the scales, whereas the field structure in OMC-2 shows no correlation across different scales. In OMC-1, the field retains its mean orientation from large to small scales but shows some deviations at small scales. Histograms of relative orientations between the magnetic field and filaments reveal a bimodal distribution for OMC-1, a relatively random distribution for OMC-2, and a distribution with a predominant peak at 90° for OMC-3. Furthermore, the magnetic fields in OMC-1 and OMC-3 both appear to be aligned perpendicular to the fibers, which are denser structures within the filament, but the field in OMC-2 is aligned along with the fibers. All these suggest that gravity, turbulence, and magnetic field are each playing a leading role in OMC-1, 2, and 3, respectively. While OMC-2 and 3 have almost the same gas mass, density, and nonthermal velocity dispersion, there are on average younger and fewer young stellar objects in OMC-3, providing evidence that a stronger magnetic field will induce slower and less efficient star formation in molecular clouds.

Unified Astronomy Thesaurus concepts: [Star formation \(1569\)](#); [Interstellar magnetic fields \(845\)](#); [Interstellar clouds \(834\)](#); [Polarimetry \(1278\)](#)

1. Introduction

During the star formation process, the dynamics and physical states of the molecular clouds are influenced by various physical mechanisms, especially self-gravity, turbulence, and magnetic field (*B*-field; C. F. McKee & E. C. Ostriker 2007). It has long been a subject of intense debate as to which force is playing a dominant role in regulating the cloud collapse and fragmentation (M.-M. Mac Low & R. S. Klessen 2004; T. C. Mouschovias et al. 2006; R. M. Crutcher 2012). Regarding the *B*-field, either the “strong-field models” that support a defining role played by the *B*-field (e.g., T. C. Mouschovias et al. 2006) or the “weak-field models” that pay more attention to turbulence (e.g., M.-M. Mac Low & R. S. Klessen 2004) cannot sufficiently explain all the observations toward star formation regions. The relative importance of turbulence and the *B*-field as well as their interactions with self-gravity in star formation remain to be explored in more case studies (H.-B. Li 2021). More reasonable scenarios may need to consider the essential roles of both processes, which have been explored in simulations (R. M. Crutcher 2012; P. Hennebelle & S. Inutsuka 2019).

Dense molecular filaments are important sites for star formation, with molecular gas accumulating and then fragmenting into star-forming cores due to gravitational instability (P. André et al. 2014; A. Hacar et al. 2023; J. E. Pineda et al. 2023). Observations have shown that *B*-fields appear to be perpendicular to high-density filaments, while they appear to be parallel to low-density elongated clouds or striations (e.g., N. L. J. Cox et al. 2016). Magnetic fields may also play a central role in shaping the fragmentation and physical states of filaments (e.g., Y.-W. Tang et al. 2019; D. Arzoumanian et al. 2021). More observations and dedicated studies are needed to reveal the relative importance of *B*-fields compared to other processes and to decipher how *B*-fields influence the gas dynamics during filament formation and fragmentation.

Situated at the head of the Orion A giant molecular cloud, the integral-shaped filament (ISF) is a well-known nearby star-forming filament (D. Johnstone & J. Bally 1999; J. Bally 2008) containing several portions, of which the more extensively studied are OMC-1, OMC-2, and OMC-3. Several studies present *B*-field results of the whole ISF (e.g., M. Houde et al. 2004; B. C. Matthews et al. 2009) or its portions OMC-1 (e.g., D. Ward-Thompson et al. 2017; D. T. Chuss et al. 2019;

H. Ajeddig et al. 2022), OMC-2/3 (F. Poidevin et al. 2010; P. S. Li et al. 2022; N. Zielinski & S. Wolf 2022), and OMC-4 (P. S. Li et al. 2022). With active massive star formation, the *B*-field in OMC-1 has been detected with a large-scale hourglass morphology associated with two molecular clumps, namely, Orion BN/KL and South (e.g., D. A. Schleuning 1998; K. Pattle et al. 2017; D. Ward-Thompson et al. 2017). The *B*-field orientations in OMC-2 exhibit more variations compared to the other portions of the ISF (e.g., F. Poidevin et al. 2010). As for OMC-3, observations have revealed a more ordered *B*-field (e.g., B. C. Matthews et al. 2001). Therefore, being the nearest filamentary molecular cloud (393 pc; J. E. Grötschdel et al. 2018) forming both massive and intermediate-to-low-mass stars, the OMC-1/2/3 region shows hints of varying *B*-field properties along the ISF, and a more comprehensive investigation is expected to provide new insights into the role of *B*-fields in filament dynamics and star formation. In this current work, as part of the *B*-fields In Star-forming Region Observations (BISTRO; D. Ward-Thompson et al. 2017; P. Bastien 2020), we use the James Clerk Maxwell Telescope (JCMT) to make submillimeter polarimetric observations of the ISF. The BISTRO team has previously observed the ISF (K. Pattle et al. 2017; D. Ward-Thompson et al. 2017). However, those observations were focused only on OMC-1. In this Letter, we have more than doubled the area studied to also include OMC-2 and 3. The aim is to set those earlier observations in the context of their environment and to understand the bigger picture of the role of magnetic fields in Orion A.

2. Observations

The observations of polarized dust emission (project ID: M17BL011, M20AL018) covering OMC-1, 2, and 3 in the Orion ISF were performed using POL-2 (P. Friberg et al. 2016) together with SCUBA-2 (W. S. Holland et al. 2013) on the JCMT. Some observations (project ID: M15BEC02) toward OMC-1 South were taken during the POL-2 commissioning stage. All the data were obtained using the POL-2 DAISY mode (P. Friberg et al. 2016).

The reduction of raw data involves three primary steps and uses two packages, SMURF and KAPPA (T. Jenness et al. 2013; M. J. Currie & D. S. Berry 2014), in the Starlink package (M. J. Currie et al. 2014). With an effective beam size of

14.''1 (~ 0.027 pc at 393 pc) at $850\ \mu\text{m}$ (J. T. Dempsey et al. 2013), we produced a synthesized map of Stokes parameters using a pixel size of 4''. We perform the absolute flux calibration with the flux conversion factor (FCF) estimated by adopting different recommended FCF values (S. Mairs et al. 2021) weighted with the observation time. In our work, FCFs were set to $695\ \text{Jy beam}^{-1}\text{pW}^{-1}$ for OMC-1 and $668\ \text{Jy beam}^{-1}\text{pW}^{-1}$ for OMC-2 and 3.

By using three models including background, source, and residual components, we smoothed the polarization maps to revise some obviously inaccurate measurements due to the uncertainty. With the calibrated Stokes parameters, the polarized intensities (PIs), polarization degrees (P), and angles (θ_P) at different positions can be calculated using the following equations:

$$\text{PI} = \sqrt{Q^2 + U^2}, \quad P = \frac{\text{PI}}{I}, \quad \text{and} \quad \theta_P = 0.5 \tan^{-1} \left(\frac{U}{Q} \right). \quad (1)$$

Since both positive and negative Q and U values contribute to a positive PI value, a modified asymptotic estimator (S. Plaszczynski et al. 2014) is employed to debias the results to avoid the overestimation of PI.

Using these equations, the parameters and their uncertainties are determined to produce a catalog of polarization half-vectors. The polarization vectors with $P/\sigma_P < 3$ or $\sigma_P > 5\%$ are removed in our analysis, where σ_P is the uncertainty of polarization degree. All the selected polarization vectors, with their lengths proportional to the polarization degrees and plotted in an interval of $8''$, are shown in Figure 1(a).

3. Results

3.1. Magnetic Field Morphology

Assuming aligned dust grains regulated by B -fields based on the radiation alignment theory (A. Lazarian 2007), the polarization angles of thermal dust emission enable one to infer the orientation of the B -field projected on the plane of the sky (PoS). Figures 1(b)–(d) show the statistics of B -field orientation distributions of the three clouds. It is clear that the B -fields in OMC-1 are mostly aligned along a northwest–southeast orientation with a position angle (PA) of about 120° , while the B -fields in OMC-3 are predominantly aligned along a northeast–southwest orientation with a PA of about 45° . On the other hand, the B -field orientations in OMC-2 have a broad distribution between 50° and 130° and another group between 0° and 30° , indicating a relatively more random distribution. In Figure 1(e), we present the half-vectors rotated by 90° in an interval of $20''$ representing the corresponding B -field orientations across the filament.

OMC-1. Overall, the B -field appears to be perpendicular to the main axis of the cloud/filament. OMC-1 is associated with the Orion Nebula Cluster (ONC) and contains a high concentration of gas at a high temperature of $>100\ \text{K}$ (e.g., D. Li et al. 2020). The maximum $850\ \mu\text{m}$ brightness of OMC-1 is approximately $9 \times 10^5\ \text{mJy beam}^{-1}$ and is associated with the hot, high-mass star-forming clumps of Orion BN/KL. Moreover, as one approaches the location of Orion BN/KL, the hourglass pattern of the B -field becomes more prominent. This pinched morphology in the central cloud of OMC-1 indicates a strong interaction between gravity and the B -field, showcasing the effects of the B -field in high-mass star-forming regions. Figure 1 also shows B -field lines that are aligned parallel with the orientation of the cloud extension in the northeastern

subfilament of OMC-1, suggesting a gas accumulation process that is guided by the B -field surrounding the filament.

OMC-2. Our dust polarization map of OMC-2 is a marked improvement over previous observations, such as the SCUPOL results (F. Poidevin et al. 2010). As a site for intermediate-to-low-mass star formation, OMC-2 seems to have relatively chaotic B -field structures compared to the other two clouds. From Figure 1(e), the B -field lines seem to converge toward denser areas in the central parts of OMC-2, where gravitational contraction is likely taking place. In contrast, a subfilament to the west of the main filament is overall perpendicular to the B -field.

OMC-3. OMC-3 appears to be a filamentary cloud extending from southeast to northwest. The POL-2 observations reveal a nearly uniform B -field in the northern backbone of OMC-3. However, the OMC-3 South, which is suspected to be a “second filament” as noted by F. Poidevin et al. (2010), has disorderly B -field directions that are similar to the complicated structures of OMC-2. In the main body of OMC-3 north, the B -field orientations are orthogonal to the filament direction. In brief, OMC-3 exhibits very ordered to even uniform B -field structures.

3.2. Multiscale View of B-field Geometries in Orion ISF

We utilized the 353 GHz polarization observations made with the High Frequency Instrument on Planck to infer the large-scale B -field (Planck Collaboration et al. 2015). The Stokes I , Q , and U maps, which were corrected for the contamination from the cosmic microwave background and cosmic infrared background, were used to generate the large-scale polarization map at a resolution of $5'$. Figure 2(a) displays the large-scale B -field maps around the Orion A region. The B -field is roughly perpendicular to the ISF. Moreover, the field structure appears slightly pinched toward the filament.

In addition, we check the optical starlight polarization observations to further explore the large-scale B -field in relatively low-density regions (F. Poidevin et al. 2011). To limit our analysis to sources within the Orion cloud, we only consider starlight detections that fall within the region of our JCMT observations and have a distance of 360–500 pc based on Gaia parallax measurements (S. Rezaei et al. 2020; C. A. L. Bailer-Jones et al. 2021; Gaia Collaboration et al. 2021). The B -fields derived from 61 detections are shown in Figure 2(b). The majority of the B -field half-vectors have a west–east or northeast–southwest orientation, in general consistent with the Planck results. Given that the optical polarization data are presumably tracing the B -field threading the ISM around the ISF or that in the foreground toward the ISF, the B -field structure shows a small deviation compared to that seen in the Planck map.

The TADPOL survey (C. L. H. Hull et al. 2014) mapped the B -fields toward several selected sources in the ISF, including Orion KL in OMC-1, FIR 3 and FIR 4 in OMC-2, and MMS 5 and MMS 6 in OMC-3, at an angular resolution of $2''.5$ (0.005 pc) using the Combined Array for Research in Millimeter-wave Astronomy (CARMA). From Figures 2(c)–(e), for OMC-1, the orientation of the small-scale B -field revealed by CARMA largely follows that of the intermediate-scale B -field seen by the JCMT POL-2, though a small fraction of the CARMA B -field half-vectors are offset from parallel to even perpendicular to the JCMT B -field half-vectors; for OMC-2, the small-scale B -field is apparently decoupled from that on the intermediate scale, and there is no obvious correlation between the orientations of the B -fields on the two scales; for OMC-3, the small-scale and intermediate-scale B -fields both

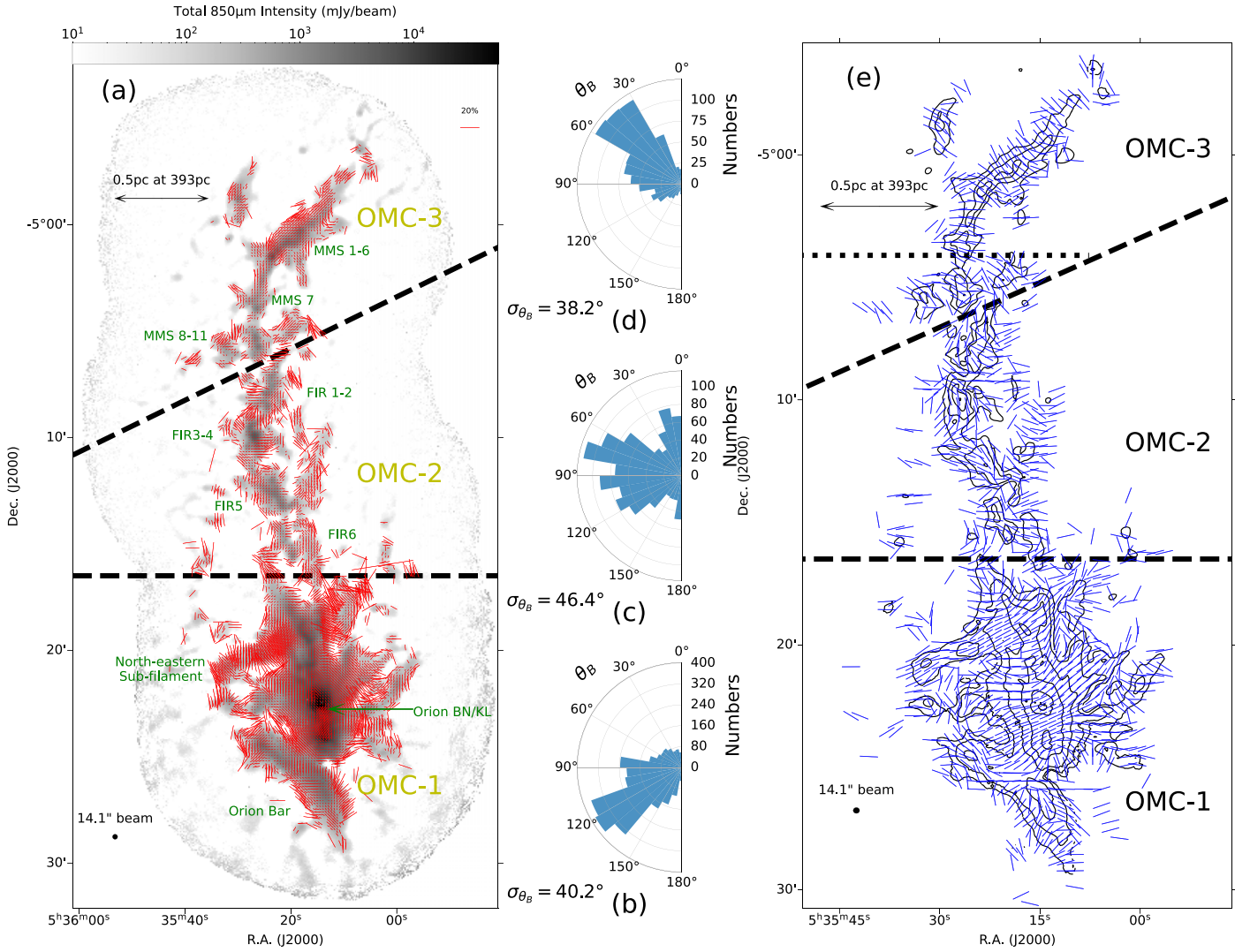


Figure 1. Panel (a): dust polarization observations of Orion A ISF made with the POL-2 on JCMT. The gray-scale image shows the $850 \mu\text{m}$ total intensity (Stokes I). Red vectors are plotted in an interval of $8''$, showing the polarization angles with the length proportional to the polarization degree. Black dashed lines mark the divisions between three clouds, i.e., OMC-1 to the south, OMC-2 in the middle, and OMC-3 to the north. The locations of the 1.3 mm sources identified by R. Chini et al. (1997), including MMS 1–10 in OMC-3, FIR 1–6 in OMC-2, and the northeastern subfilament and Orion Bar in OMC-1, are marked on the image. Panels (b), (c), and (d) show the histograms of the PAs of the B -field orientations for OMC-1, OMC-2, and OMC-3, respectively. Panel (e): blue vectors with a uniform arbitrary length are plotted in an interval of $20''$, showing the magnetic field orientations, and are derived by rotating the polarization vectors by 90° . The $850 \mu\text{m}$ total intensity is shown in black contours at log₁₀ scale (mJy beam⁻¹), which starts from 2.2 and continues in steps of 0.5. The black dotted line splits the OMC-3 cloud into the North and South parts.

appear to be uniform with almost the same orientation. There have been new Atacama Large Millimeter/submillimeter Array (ALMA) observations of dust polarization toward several sources in the ISF; however, these observations were made at subarcsecond resolutions, either probing B -field structures at too-small scales to be compared with the JCMT data (P. C. Cortes et al. 2021) or being dominated by self-scattering and thus unable to probe the B -field structure (S. Takahashi et al. 2019; Y. Liu et al. 2024).

More quantitatively, we compare the intermediate-scale B -field probed by JCMT POL-2 with the large-scale B -field probed by Planck by calculating the difference angle, $\Delta\theta_B$, between the orientations of the B -fields on the two scales. Since the Planck map covers an area much larger than what is covered by the JCMT map, we calculate $\Delta\theta_B$ for each half-vector at $8''$ intervals in the JCMT map; the B -field orientation at the corresponding position in the Planck map is derived by a weighted average of the B -field orientations at the nearest 4

pixels, where the pixel size of the Planck map is $2'$ and the weighting is taken as the inverse of the square of the distance between the pixel center to the position of interest. In Figure 2(f), the histogram of $\Delta\theta_B$ for OMC-1 is clearly peaking toward 0° , suggesting that the orientation of the intermediate-scale (0.03 pc) B -field is predominantly parallel with that of the large-scale (0.6 pc) B -field. For OMC-2, $\Delta\theta_B$ appears to be widely distributed between 0° and 90° , with a very minor tendency of peaking at 0° , indicating that the B -field orientation on the intermediate scale has shown strong local variation and started to decouple from that on the large scale. For OMC-3, $\Delta\theta_B$ are almost all below 35° , indicating that the intermediate-scale B -field is well aligned with that on the large scale.

Similarly to $\Delta\theta_B$, we compute the difference angle, $\delta\theta_B$, between the orientations of the B -fields probed by JCMT and CARMA for each CARMA detection. Again, the B -field orientation at the corresponding position in the JCMT map is

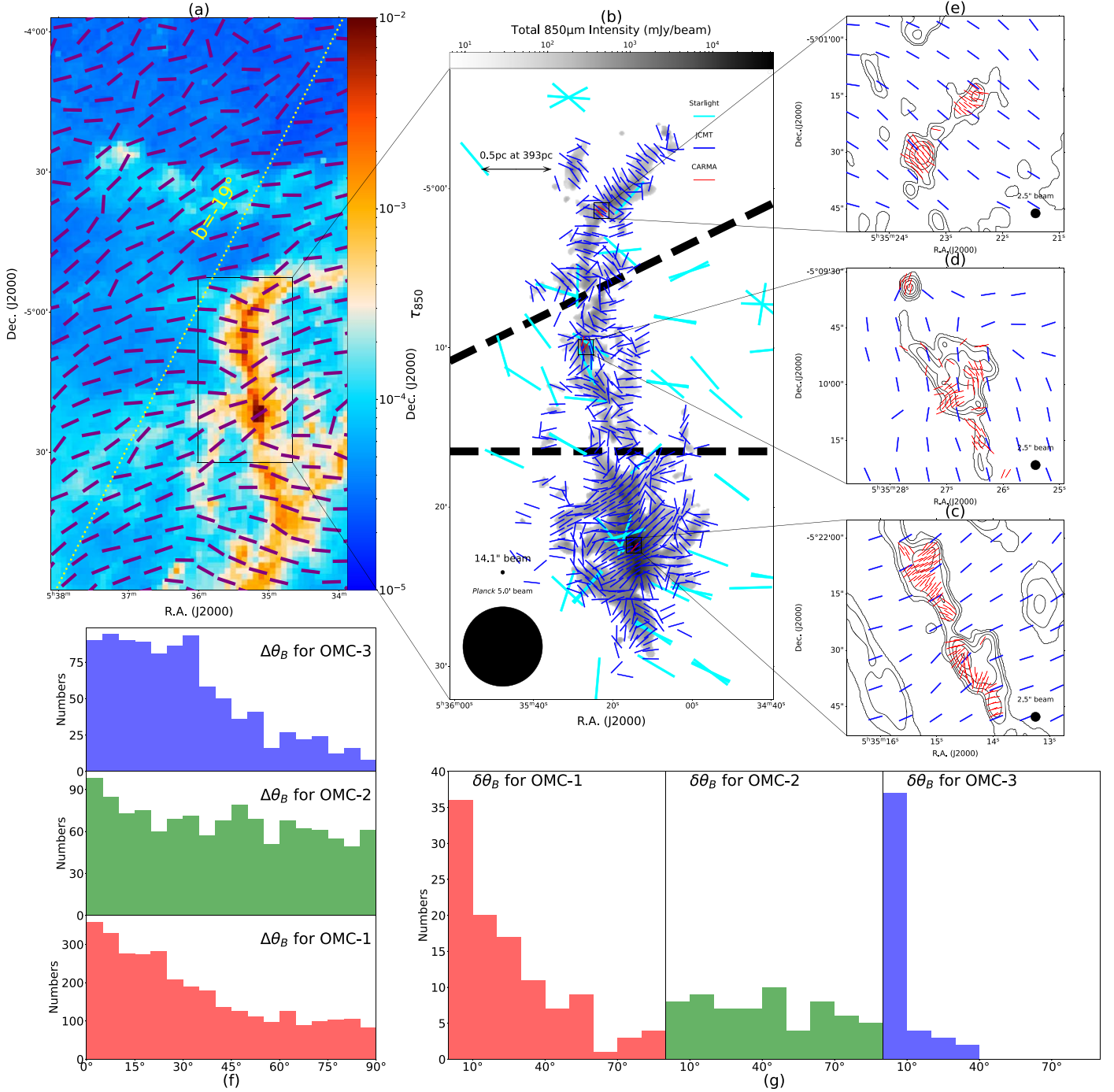


Figure 2. Multiscale B -field orientations in the ISF. Panel (a): the background image displays the 850 μm opacity map obtained from the Herschel and Planck data (M. Lombardi et al. 2014); purple segments indicate the large-scale B -field orientations inferred from the Planck 353 GHz data. A yellow dotted line marks the galactic latitude $b = 19^\circ$. Panel (b): B -field orientations derived from starlight, JCMT POL-2, and CARMA observations. The background image shows the JCMT 850 μm total intensity map; blue vectors plotted at an interval of $32''$ denote the B -field orientations observed by JCMT POL-2, cyan vectors represent the B -field orientations revealed by starlight polarization observations (F. Poidevin et al. 2011), and red vectors show the averaged B -field orientations obtained by the CARMA TADPOL survey (C. L. H. Hull et al. 2014). In panels (c), (d), and (e), red vectors indicate the B -field orientations obtained by the CARMA TADPOL survey in selected dense cores located in OMC-1, OMC-2, and OMC-3, respectively; blue vectors show the B -field orientations derived with the JCMT POL-2 observations; and the CARMA observations of the total dust emission at 1.3 mm are shown in black contours at \log_{10} scale (mJy beam^{-1}), which starts from -2.0 and continues in steps of 0.5 in panel (c), starts from -2.0 and continues in steps of 0.2 in panel (d), and starts from -1.0 and continues in steps of 0.3 in panel (e). Panel (f): histograms of the difference angles between the B -field orientations unveiled by Planck and that by the JCMT POL-2 for OMC-1, OMC-2, and OMC-3. Panel (g): histograms of the difference angles between the B -field orientations obtained by the JCMT POL-2 and by the CARMA TADPOL survey for OMC-1, OMC-2, and OMC-3.

derived by a weighted average of the B -field orientations at the nearest 4 pixels, and the weighting is taken as the inverse of the square of the distance between the pixel center to the position of interest. In Figure 2(g), the distribution of $\delta\theta_B$ for OMC-1 shows a clear peak at 0° – 10° and gradually declines

toward 90° ; for OMC-2, $\delta\theta_B$ has a nearly flat distribution, again indicating that the B -fields on the two scales are apparently decoupled; for OMC-3, the distribution of $\delta\theta_B$ depicts that the B -field orientations almost do not change across the two scales.

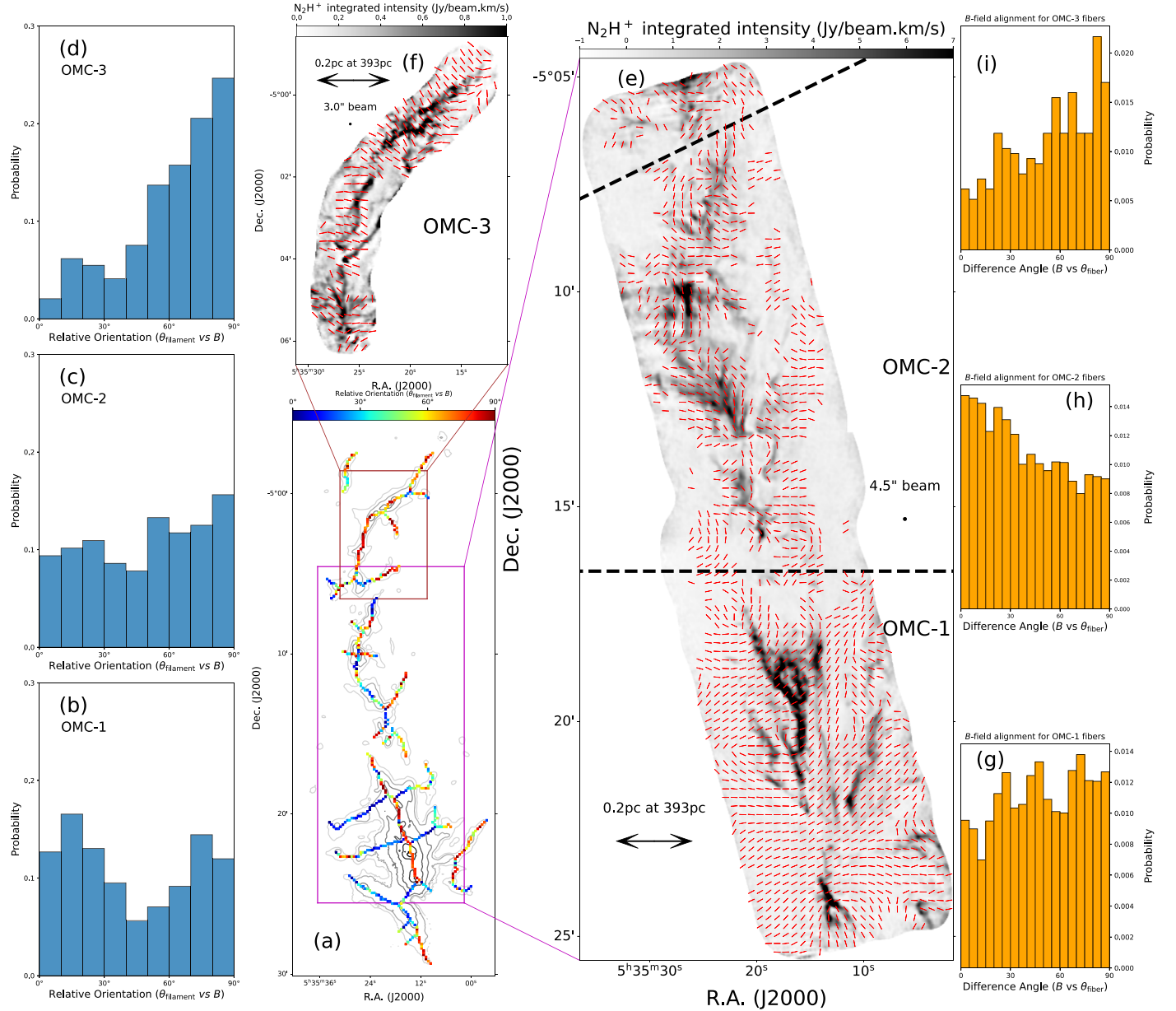


Figure 3. Panel (a): colored points show locations along the skeleton of each filament where the filament orientation is compared with the B -field orientation, and the color scale denotes the derived difference angle between the two orientations, as indicated by a color bar on the top; the $850\ \mu\text{m}$ total intensity is shown in contours with levels at a \log_{10} scale (mJy beam^{-1}), starting from 2.2 and continuing at steps of 0.5. Panels (b), (c), and (d): histograms of the difference angles between the filament skeleton and B -field orientations for OMC-1, OMC-2, and OMC-3. Panel (e): red vectors plotted at an interval of $12''$ show the B -field orientations derived by the JCMT POL-2, and the gray-scale image shows the N_2H^+ (1–0) velocity-integrated emission in OMC-1 and OMC-2 (A. Hacar et al. 2018). Panel (f): same as panel (e) but for OMC-3, and the N_2H^+ data are taken from C. Zhang et al. (2020). Panels (g), (h), and (i) show the histograms of the difference angles between the N_2H^+ fibers and POL-2 B -field orientations in OMC-1, OMC-2, and OMC-3, respectively.

3.3. Relations between B-field and Filamentary Structures

To investigate how the B -field orientation is aligned with the filamentary structures in the ISF, we employed the *filfinder* algorithm (E. W. Koch & E. W. Rosolowsky 2015) to extract filament skeletons. Figure 3(a) shows the derived skeletons along the main filament, the branches connected to the main filament, and some minor structures detached from the main filament. To quantify the filament orientations, we utilize the principal component analysis method on 10 adjacent pixels of the skeletons to determine the PA of the filaments at each position. We then compute the difference angles between the filament and B -field orientations. In Figure 3(a), the color scale of the skeletons visualizes the spatial distribution of the

difference angles. Figures 3(b)–(d) show the histograms of the difference angles for OMC-1, OMC-2, and OMC-3, respectively. Along the filamentary cloud, three drastically different distributions for the relative orientation between the B -fields and filaments are seen: a bimodal distribution for OMC-1, nearly flat distribution for OMC-2, and a distribution with a predominant single peak at 90° for OMC-3. From the skeleton color scale representing the difference angles (Figure 3(a)), we can see that the bimodal distribution in OMC-1 is due to a combined effect that along the main filament, the B -field orientation is perpendicular to the filament axis, while along the relatively low-density branches, the B -field orientation is parallel to the branch axis; on the other hand,

for the distribution of relative orientation in OMC-3, a tail toward 0° is mostly attributed to OMC-3 South.

Molecular filaments may have complex internal structures, such as intertwined filamentary bundles or fibers. We identified the fibers with the filfinder algorithm from N_2H^+ maps (see Appendix A). Figure 3(e) shows a comparison between the B -field orientations derived from our POL-2 observations and the fiber structures revealed by the combined ALMA and IRAM 30 m N_2H^+ (1–0) observations of OMC-1 and 2 (A. Hacar et al. 2018). Such a comparison for OMC-3 is shown in Figure 3(f), where the ALMA N_2H^+ (1–0) data were taken from C. Zhang et al. (2020). We calculate the difference angles between the fiber and B -field orientations, as shown in Figures 3(g)–(i). In OMC-1, the fibers tend to be perpendicular to the B -field; this is not difficult to understand considering the bimodal distribution for the relative orientation between the B -field and filaments (Figure 3(b)), and here the fibers traced by the N_2H^+ emission represent the high-density part of the filaments. In OMC-3, the fibers are clearly perpendicular to the B -field, consistent with the distribution of relative orientation between the B -field and filaments. Interestingly, the fibers in OMC-2 appear to be predominantly parallel to the B -field, in contrast to the random distribution of relative orientation between the B -field and filaments.

4. Discussion and Summary

4.1. A Tale of Three: Gravitational, Turbulent, and Magnetic Interpretations for OMC-1, 2, and 3, Respectively

We have presented JCMT POL-2 dust polarization observations of a remarkable molecular filament containing OMC-1, OMC-2, and OMC-3 in the Orion ISF. Combining the POL-2 data with the Planck and CARMA polarization observations, we clearly see how the B -fields vary from the large (~ 0.6 pc) to intermediate (~ 0.03 pc) and small (~ 0.005) scales: for OMC-1, the B -field retains its mean orientation on all the scales, with some local variations on intermediate-to-small scales; for OMC-2, the B -fields on different scales are apparently decoupled, showing relatively disordered morphology on the intermediate and small scales; and for OMC-3, the B -field shows a uniform morphology, and the orientation does not change all the way from the large to intermediate and small scales. A natural and straightforward interpretation of such B -field morphologies, in particular their variation across different scales, is that the B -field in OMC-1 is channeling the gas accretion from the ambient medium to the filament, but as the mass continues to grow, forming massive dense cores within the filament, gravity overcomes the magnetic force, pulling the B -field into an hourglass shape (see also K. Pattle et al. 2017; D. Ward-Thompson et al. 2017). The B -field in OMC-2 appears highly twisted on intermediate and small scales, suggesting that turbulence is dominating over the B -field; the B -field in OMC-3, especially OMC-3 North, has a nearly uniform morphology from large to small scales, indicating that the B -field is strong enough to dominate the gas dynamics (e.g., E. C. Ostriker et al. 2001). Below, we test this simple interpretation by comparing the orientations between the B -fields and the dense gas structures.

Filamentary clouds naturally define an axis to be compared to the B -field, and such a comparison for ISF again reveals a trio: bimodal for OMC-1, random for OMC-2, and perpendicular for OMC-3 (Figures 3(b)–(d)). It immediately renders strong support to the above ternary interpretation. The

bimodal distribution for the relative orientation between the B -field and filaments in OMC-1 is clearly correlated to the gas density, with the high-density filament skeleton perpendicular to the B -field and low-density skeletons parallel to the B -field, consistent with the scenario that the B -field is channeling gas flows toward the high-density filament (e.g., D. Ward-Thompson et al. 2017; T. G. S. Pillai et al. 2020; P. Girichidis 2021). Such a correlation is strengthened by looking into the filament internal structures, i.e., the N_2H^+ fibers: as the high-density part of the filament, the fibers are preferentially perpendicular to the B -field (Figure 3(g)). In OMC-2, the random distribution is apparently a consequence of the disordered nature of the B -field structure. Very interestingly, the fibers in OMC-2 are largely parallel to the B -field (Figure 3(h)), showing a pattern that is consistent with the results of simulations of super-Alfvénic turbulence (see, e.g., Figures 2 and 3 in P. Padoan et al. 2001), suggesting that turbulence is dynamically more important than the B -field in OMC-2. For OMC-3, the B -field is simply perpendicular to both the filament (Figure 3(d)) and fibers (Figure 3(i)), indicating that the B -field is strong enough to counteract gravity and turbulence.

4.2. The B -field Strength Estimates

To further quantify the impact of the B -field on the dynamical evolution of the filament, it is desirable to estimate the B -field strength. However, deriving the B -field strength with the David–Chandrasekhar–Fermi (DCF) method (L. Davis 1951; S. Chandrasekhar & E. Fermi 1953) or its variants is subject to large uncertainty and in some cases is not applicable (J. Liu et al. 2021, 2022a, 2022b; C.-Y. Chen et al. 2022). First, the method requires calculating the polarization angle dispersion due to turbulent disturbance, or decomposing the B -field into turbulent and ordered components and calculating their ratio. This step is not always feasible, especially when the B -field structure is complicated. Second, under the assumption of energy equipartition between turbulence and the turbulent B -field, and adopting a gas density and turbulent velocity dispersion obtained from other observations, the PoS B -field strength can be derived. It should be noted that the energy equipartition assumption may not be valid when the B -field is weak. The estimates of the gas density and turbulent velocity dispersion often suffer large uncertainties. Nevertheless, the method has been widely used. Several such estimates for the sources in the ISF exist in the literature, and the results vary a lot, ranging from 0.3 to 6.6 mG for OMC-1 and from 0.13 to 0.64 mG for OMC-3 (B. C. Matthews et al. 2005; J. P. Vallée & J. D. Fiege 2007; R. H. Hildebrand et al. 2009; M. Houde et al. 2009; F. Poidevin et al. 2013; K. Pattle et al. 2017; D. T. Chuss et al. 2019; J. A. Guerra et al. 2021; J. Hwang et al. 2021; P. S. Li et al. 2022; N. Zielinski & S. Wolf 2022). Here we try with the best effort to estimate the PoS B -field strengths in the three regions with the new data, obtaining 0.45, 0.25, and 0.37 mG for OMC-1, 2, and 3, respectively (see Appendix B).

Given the aforementioned cautions and uncertainties, we only make a comparative rather than a more detailed quantitative analysis based on the derived B -field strengths. It is worth mentioning that OMC-1 has a width about 2 times greater than OMC-2 and 3 under the same column density threshold, resulting in a volume density in this region slightly lower than that in the latter two. But about half of the gas mass

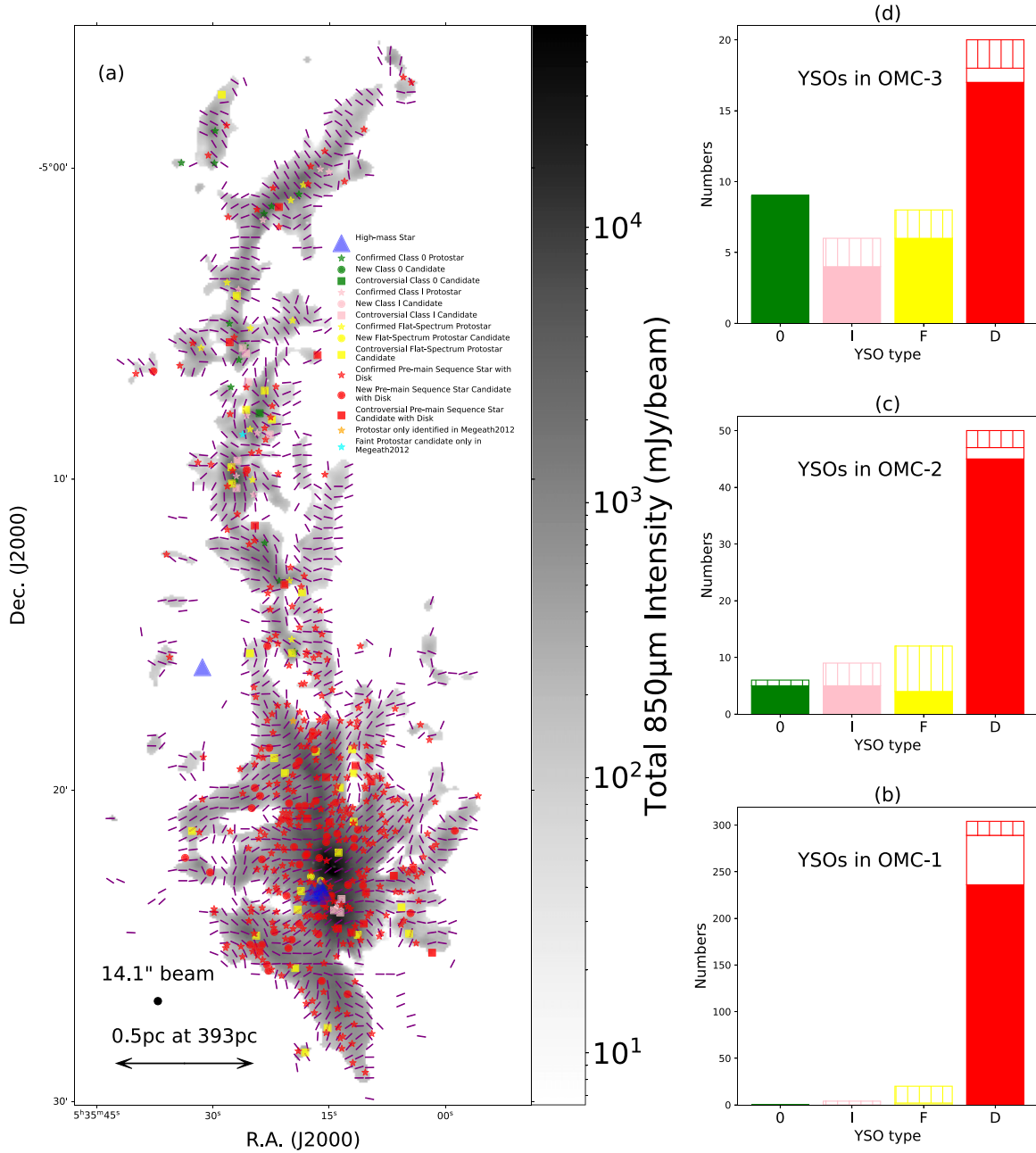


Figure 4. Panel (a): distribution of detected YSOs overlaid on the B -field orientation maps. All the YSO candidates and high-mass stars are taken from the literature (S. T. Megeath et al. 2012; E. Furlan et al. 2016; J. E. Großschedl et al. 2019). Purple vectors at a $20''$ interval indicate the B -field orientations observed by the JCMT POL-2. The class 0, class I, flat-spectrum sources, and pre-main-sequence stars with disks are denoted in green, pink, yellow, and red colors, respectively. For each YSO type, the confirmed ones that are consistent in different literature are represented by star symbols; newly discovered candidates by J. E. Großschedl et al. (2019) are indicated with filled circles; controversial candidates, showing inconsistencies in different literature, are marked with filled squares. Panels (b), (c), and (d): histograms of the four YSO types in OMC-1, OMC-2, and OMC-3, respectively; class 0, class I, flat-spectrum sources, and pre-main-sequence stars with disks are labeled as “0,” “I,” “F,” and “D,” respectively, with the same colors as in panel (a); filled histograms represent confirmed YSOs, open histograms depict newly discovered YSOs, and vertical gridded histograms indicate controversial YSOs.

in OMC-1 is attributed to the central high-density part with a width of ~ 0.06 pc, and within that area, the average volume density reaches $2.5 \times 10^6 \text{ cm}^{-3}$. Therefore, though the B -field in OMC-1 is stronger, considering a much greater mass and central density, it is completely plausible that gravity is overwhelmingly more important in this region. OMC-2 and 3 have almost the same mass and nonthermal velocity dispersion (see Appendix B), while the B -field in OMC-3 is stronger than that in OMC-2; the relative B -field strength of the two regions is at least compatible with the interpretation that turbulence in OMC-2 and the B -field in OMC-3 are taking a leading role.

4.3. The Impact of the Magnetic Field on Star Formation

Given the markedly different B -field properties across the three regions in the ISF, it is of great interest to examine how the star formation activity is affected. We collect a catalog of young stellar objects (YSOs), which are classified into class 0, class I, flat-spectrum, and disk-bearing pre-main-sequence stars, based on the works of S. T. Megeath et al. (2012), E. Furlan et al. (2016), and J. E. Großschedl et al. (2019). Figure 4 shows all the YSOs in OMC-1, 2, and 3 and the statistics of each type in each of the three regions. The star

formation activity in OMC-1 is far more vigorous and complicated than that in OMC-2 and 3. OMC-1 is the only region of the three forming high-mass stars, containing several well-known high-mass protostellar objects. It is located behind the luminous Trapezium cluster, which is the central part of the ONC. The collected YSOs in this region are completely dominated by the disk sources and are heavily contaminated by the foreground ONC sources (C. J. Lada et al. 2000; J. Otter et al. 2021). Here we focus on the comparison between OMC-2 and OMC-3. From Figure 4, OMC-2 has a higher fraction of disk sources (50/78) than OMC-3 (20/43), indicating a younger age of the cluster in OMC-3. The total number of YSOs in OMC-2 is higher than that in OMC-3. Note that the mass, mean density, and nonthermal velocity dispersion in the two regions are almost the same, and the only appreciable difference lies in the B -field geometries and the relative orientation between the B -fields and filaments/fibers. Therefore, the differing YSO populations in the two regions are mostly likely due to the B -field effect, providing compelling evidence that a dynamically more important B -field leads to slower (or delayed) and less efficient star formation in molecular clouds.

To summarize, concerning which mechanism is shaping the dynamics of molecular clouds on ~ 0.01 – 1 pc scales, each of the three clouds (OMC-1, 2, and 3 in the Orion ISF) seems to be telling a different story based on our JCMT POL-2 observations along with the Planck and CARMA data. Therefore, it is probably an oversimplified interpretation to claim that either the magnetic field or turbulence is universally more important in molecular cloud evolution and star formation. By comparing the YSO populations in OMC-2 and 3, we find evidence that a strong B -field could make star formation relatively slower and less efficient. Y. Zhang et al. (2019) carried out MHD simulations of sub-Alfvénic molecular clouds, focusing on the B -field orientation variation across various scales. They found that on small (< 0.1 pc) scales, the cores are super-Alfvénic as a consequence of turbulent energy concentration induced by gravity, and thus the B -field on small scales exhibits a wide range of deviation in orientation from that on large scales. If one takes an average B -field orientation for each of the dense cores in the CARMA maps (Figures 2(c)–(e)) and compares to the B -field revealed by Planck, the offset distribution could be to some extent consistent with the work of Y. Zhang et al. (2019). However, a detailed comparison shows that the cross-scale correlation in B -field orientation (Figures 2(f) and (g)) is distinctly different from region to region, certainly not random in OMC-1 and 3. The observed relation between the B -field and filament/fiber orientations and the star formation activity variation further suggests a tale-of-three interpretation of the three regions regarding the interplay between gravity, B -fields, and turbulence.

Acknowledgments

This work is supported by the National Natural Science Foundation of China (NSFC) grant Nos. 12425304 and U1731237, the National Key R&D Program of China with Nos. 2023YFA1608204 and 2022YFA1603103, and the science research grant from the China Manned Space Project with No. CMS-CSST-2021-B06. J.W. thanks Chao Zhang, Nan-Nan Yue, Di Li, and Qizhou Zhang for generously providing us the N_2H^+ data that covered OMC-2 and OMC-3 in Orion for the analysis of fiber structures. K.P. is a Royal Society University Research Fellow, supported by Grant No. URF\R1\211322. D.J. is supported by NRC Canada and by an NSERC Discovery Grant. C.W.L. acknowledges support from the Basic Science Research Program through the NRF funded by the Ministry of Education, Science and Technology (NRF-2019R1A2C1010851) and by the Korea Astronomy and Space Science Institute grant funded by the Korea government (MSIT; project No. 2024-1-841-00). W.K. was supported by the National Research Foundation of Korea (NRF) grant funded by the Korea government (MSIT; RS-2024-00342488). S.P.L. acknowledges grants from the National Science and Technology Council of Taiwan, under project numbers 109-2112-M-007-010-MY3, 112-2112-M-007-011, and 113-2112-M-007-004. The work of M.G.R. is supported by the international Gemini Observatory, a program of NSF NOIR-Lab, which is managed by the Association of Universities for Research in Astronomy (AURA) under a cooperative agreement with the U.S. National Science Foundation, on behalf of the Gemini partnership of Argentina, Brazil, Canada, Chile, the Republic of Korea, and the United States of America. C.E. acknowledges the financial support from the grant RJF/2020/000071 as a part of the Ramanujan Fellowship awarded by the Science and Engineering Research Board (SERB). The James Clerk Maxwell Telescope is operated by the East Asian Observatory on behalf of The National Astronomical Observatory of Japan, the Academia Sinica Institute of Astronomy and Astrophysics, the Korea Astronomy and Space Science Institute, and the Center for Astronomical Mega-Science (as well as the National Key R&D Program of China with No. 2017YFA0402700). Additional funding support is provided by the Science and Technology Facilities Council of the United Kingdom and participating universities in the United Kingdom, Canada, and Ireland. Additional funds for the construction of SCUBA-2 and POL-2 were provided by the Canada Foundation for Innovation.

Appendix A Identified Fiber Structures

The fibers within the filament are extracted using the filfinder algorithm from the N_2H^+ (1–0) velocity-integrated emission maps. Figure 5 shows a comparison between the derived fibers, the N_2H^+ emission, and the total 850 μm emission.

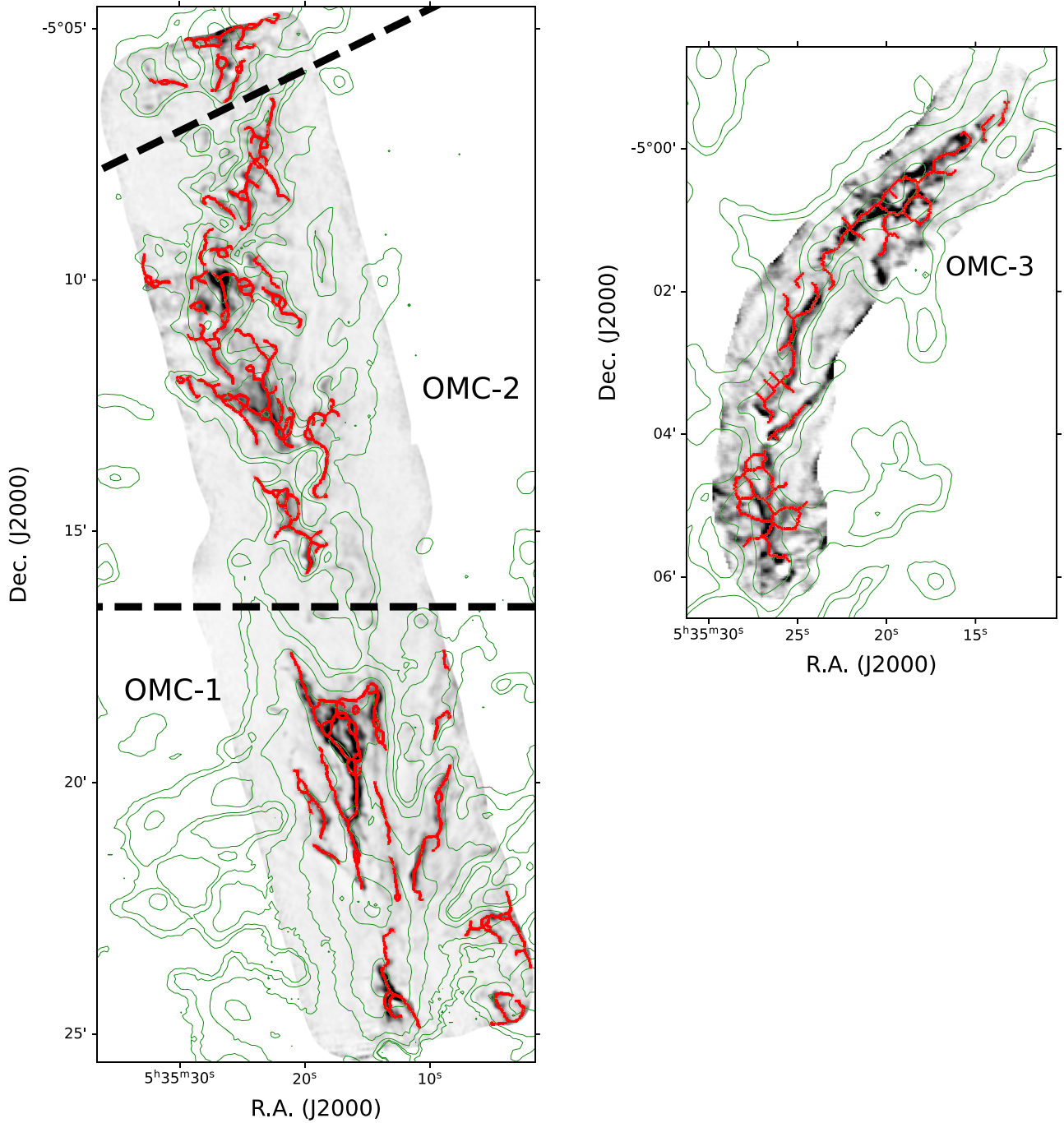


Figure 5. Gray-scale images show the velocity-integrated N_2H^+ (1–0) emissions, overlaid with the extracted fibers shown in red lines and the total $850\ \mu\text{m}$ intensity shown in green contours. The left panel shows the OMC-1 and 2 region, with the N_2H^+ data taken from A. Hacar et al. (2018), and the right panel shows OMC-3, with the N_2H^+ data taken from C. Zhang et al. (2020).

Appendix B Details for B -field Strength Calculation

In the DCF assumption, the PoS B -field strength of the molecular cloud is estimated by interpreting the observed deviation of polarization angles from a mean polarization angle distribution as a result of Alfvén waves induced by turbulent perturbations, i.e.,

$$B_0 = \sigma_v \sqrt{\mu_0 \rho} \left(\frac{\delta B}{B_0} \right)^{-1}, \quad (\text{B1})$$

where σ_v represents the turbulence-induced velocity dispersion that could approximately equate to the nonthermal velocity dispersion and ρ denotes the gas mass density. $\delta B/B_0$ denotes the turbulent-to-ordered magnetic field ratio.

To obtain the mass density, we modeled the three star-forming clouds within the Orion A ISF as cylindrical filaments. We use the column density map at $\sim 8''$ resolution produced by F. Schuller et al. (2021) to measure the mass of the three regions, obtaining ~ 660 , ~ 250 , and $\sim 260\ M_\odot$ for OMC-1, 2, and 3. The dimensions of the three regions are measured to be approximately $0.93\ \text{pc} \times 0.23\ \text{pc}$ for OMC-1, $1.0\ \text{pc} \times 0.1\ \text{pc}$

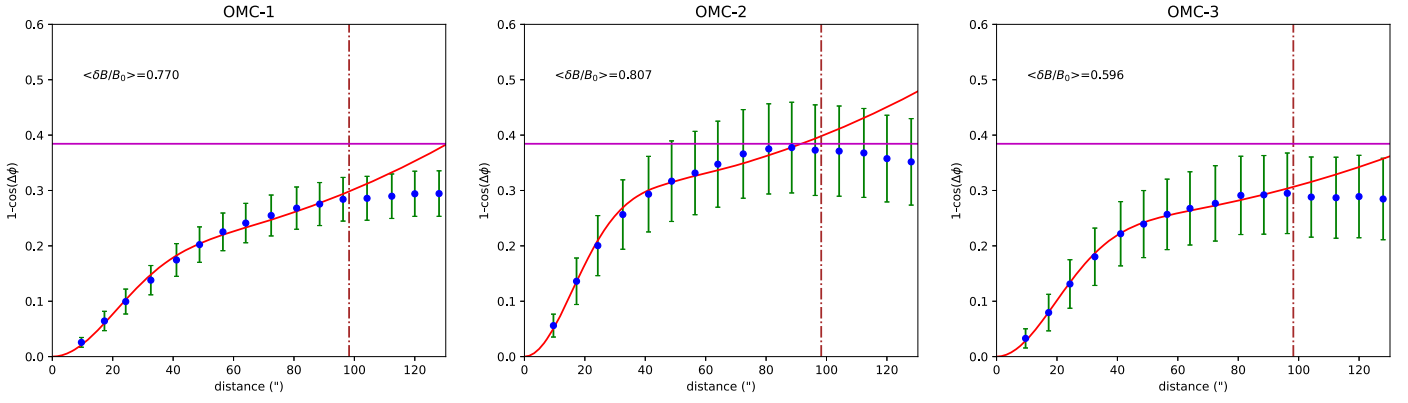


Figure 6. Fitting results of the ACF for OMC-1, 2, and 3 from left to right. For each panel, blue filled circles with error bars denote data points derived from the polarization observations, the best-fitting result is shown by a red solid line, a horizontal magenta line marks the value expected for a random field (52°; F. Poidevin et al. 2010), and a vertical brown dashed-dotted line marks the right boundary of the points to be fitted.

for OMC-2, and $1.0 \text{ pc} \times 0.1 \text{ pc}$ for OMC-3. Assuming a cylinder geometry lying in the PoS, the volume densities are found to be $\sim 2.4 \times 10^5$, $\sim 4.5 \times 10^5$, and $\sim 4.7 \times 10^5 \text{ cm}^{-3}$ for OMC-1, 2, and 3, respectively.

To estimate the velocity dispersion in the ISF, we utilized the NH_3 (1, 1) observation data from the Green Bank Ammonia Survey (R. K. Friesen et al. 2017) with a resolution of $36''$. To extract the nonthermal velocity dispersion, we subtracted the thermal components of the observed velocity dispersion with the temperature map provided by F. Schuller et al. (2021). Our analysis revealed that the mean nonthermal velocity dispersion in OMC-1, OMC-2, and OMC-3 is 0.90 km s^{-1} , 0.38 km s^{-1} , and 0.41 km s^{-1} , respectively.

The turbulent-to-ordered magnetic field ratio $\delta B/B_0$ is determined by the dispersion of polarization angles. However, quantifying the turbulent B -field components could have bias due to the effects of nonturbulent field structure in dense clouds. So the angular dispersion function method has been developed to reduce the bias. Moreover, by considering the effect of signal integration along the line of sight and within the beam in the analysis, M. Houde et al. (2009) proposed the autocorrelation function (ACF) form to precisely derive the turbulent-to-ordered magnetic field ratios. The angular dispersion function could be expressed as

$$1 - \langle \cos[\Delta\Phi(l)] \rangle \simeq \frac{1}{N} \frac{\langle \delta B^2 \rangle}{\langle B_0^2 \rangle} \times [1 - e^{-l^2/2(\delta^2 + 2W^2)}] + a_2 l^2, \quad (\text{B2})$$

where N is the number of turbulent cells probed by the telescope beam, $\Delta\Phi(l)$ represents the PA differences of two vectors at a distance l , a_2 signifies the slope of the second-order term in the Taylor expansion,

$$N = \frac{(\delta^2 + 2W^2)\Delta'}{\sqrt{2\pi}\delta^3}, \quad (\text{B3})$$

W denotes the beam radius (6.0 for JCMT $850 \mu\text{m}$ observations), Δ' depicts the cloud depth, and δ stands for the turbulent correlation length.

Setting cloud depths to 0.23 pc , 0.1 pc , and 0.1 pc for OMC-1, OMC-2, and OMC-3, respectively, we derived the ACF of the three clouds with the JCMT POL-2 polarization vectors (2952 vectors in OMC-1, 1118 vectors in OMC-2, 890 vectors

in OMC-3). Equation (B2) is valid when l is not too big compared to a few times of W (M. Houde et al. 2009). In addition, we have a polarization map with a finite size, and thus the number of polarization detections on which the ACF could be derived at high intensities decreases as l increases, leading to degrading statistics for the data points on large l . We therefore limit our fitting to the data points with $l < 100''$. In Figure 6, the fitting results revealed that OMC-3 has the smallest $\delta B/B_0$ value of 0.596, and OMC-2 has the largest $\delta B/B_0$ value of 0.807, while OMC-1 has a $\delta B/B_0$ value of 0.770. We also obtain $\delta = 4.39$, 3.15 , and 4.08 mpc for OMC-1, 2, and 3, respectively, with the fitting. We note that δ cannot be resolved with a telescope beam of 27 mpc ($14''$ at a distance of 393 pc). Such an issue occurs in other works applying the ACF fitting to dust polarization data (e.g., M. Houde et al. 2009; K. Qiu et al. 2013). Thus, the inferred δ is more like a numerical artifact from the fitting, and the turbulence correlation scale is still to be explored. We finally estimated the strength of the PoS component of the B -field for OMC-1, OMC-2, and OMC-3 as 0.45 mG , 0.25 mG , and 0.37 mG , respectively.

ORCID iDs

Jintai Wu <https://orcid.org/0000-0001-7276-3590>
 Keping Qiu <https://orcid.org/0000-0002-5093-5088>
 Frédéric Poidevin <https://orcid.org/0000-0002-5391-5568>
 Pierre Bastien <https://orcid.org/0000-0002-0794-3859>
 Junhao Liu <https://orcid.org/0000-0002-4774-2998>
 Tao-Chung Ching <https://orcid.org/0000-0001-8516-2532>
 Tyler L. Bourke <https://orcid.org/0000-0001-7491-0048>
 Derek Ward-Thompson <https://orcid.org/0000-0003-1140-2761>
 Kate Pattle <https://orcid.org/0000-0002-8557-3582>
 Doug Johnstone <https://orcid.org/0000-0002-6773-459X>
 Patrick M. Koch <https://orcid.org/0000-0003-2777-5861>
 Chang Won Lee <https://orcid.org/0000-0002-3179-6334>
 Lapo Fanciullo <https://orcid.org/0000-0001-9930-9240>
 Takashi Onaka <https://orcid.org/0000-0002-8234-6747>
 Jihye Hwang <https://orcid.org/0000-0001-7866-2686>
 Valentin J. M. Le Gouellec <https://orcid.org/0000-0002-5714-799X>
 Archana Soam <https://orcid.org/0000-0002-6386-2906>
 Motohide Tamura <https://orcid.org/0000-0002-6510-0681>
 Mehrnoosh Tahani <https://orcid.org/0000-0001-8749-1436>

Chakali Eswaraiah  <https://orcid.org/0000-0003-4761-6139>
 David Berry  <https://orcid.org/0000-0001-6524-2447>
 Simon Coudé  <https://orcid.org/0000-0002-0859-0805>
 Woojin Kwon  <https://orcid.org/0000-0003-4022-4132>
 Sheng-Jun Lin  <https://orcid.org/0000-0002-6868-4483>
 Jia-Wei Wang  <https://orcid.org/0000-0002-6668-974X>
 Tetsuo Hasegawa  <https://orcid.org/0000-0003-1853-0184>
 Shih-Ping Lai  <https://orcid.org/0000-0001-5522-486X>
 Huei-Ru Vivien Chen  <https://orcid.org/0000-0002-9774-1846>
 Wen Ping Chen  <https://orcid.org/0000-0003-0262-272X>
 Eun Jung Chung  <https://orcid.org/0000-0003-0014-1527>
 James Di Francesco  <https://orcid.org/0000-0002-9289-2450>
 Pham Ngoc Diep  <https://orcid.org/0000-0002-2808-0888>
 Yasuo Doi  <https://orcid.org/0000-0001-8746-6548>
 Hao-Yuan Duan  <https://orcid.org/0000-0002-7022-4742>
 David Eden  <https://orcid.org/0000-0002-5881-3229>
 Laura M. Fissel  <https://orcid.org/0000-0002-4666-609X>
 Tim Gledhill  <https://orcid.org/0000-0002-2859-4600>
 Qilao Gu  <https://orcid.org/0000-0002-2826-1902>
 Ilseung Han  <https://orcid.org/0000-0002-9143-1433>
 Thiem Hoang  <https://orcid.org/0000-0003-2017-0982>
 Tsuyoshi Inoue  <https://orcid.org/0000-0002-7935-8771>
 Shu-ichiro Inutsuka  <https://orcid.org/0000-0003-4366-6518>
 Kazunari Iwasaki  <https://orcid.org/0000-0002-9892-1881>
 Il-Gyo Jeong  <https://orcid.org/0000-0002-5492-6832>
 Ji-hyun Kang  <https://orcid.org/0000-0001-7379-6263>
 Miju Kang  <https://orcid.org/0000-0002-5016-050X>
 Janik Karoly  <https://orcid.org/0000-0001-5996-3600>
 Shinyoung Kim  <https://orcid.org/0000-0001-9333-5608>
 Kyoung Hee Kim  <https://orcid.org/0000-0001-9597-7196>
 Kee-Tae Kim  <https://orcid.org/0000-0003-2412-7092>
 Jongsoo Kim  <https://orcid.org/0000-0002-1229-0426>
 Gwanjeong Kim  <https://orcid.org/0000-0003-2011-8172>
 Florian Kirchschlager  <https://orcid.org/0000-0002-3036-0184>
 Masato I.N. Kobayashi  <https://orcid.org/0000-0003-3990-1204>
 Jungmi Kwon  <https://orcid.org/0000-0003-2815-7774>
 Sheng-Yuan Liu  <https://orcid.org/0000-0003-4603-7119>
 Tie Liu  <https://orcid.org/0000-0002-5286-2564>
 Hong-Li Liu  <https://orcid.org/0000-0003-3343-9645>
 Xing Lu  <https://orcid.org/0000-0003-2619-9305>
 Steve Mairs  <https://orcid.org/0000-0002-6956-0730>
 Masafumi Matsumura  <https://orcid.org/0000-0002-6906-1013>
 Gerald Moriarty-Schieven  <https://orcid.org/0000-0002-0393-7822>
 Fumitaka Nakamura  <https://orcid.org/0000-0001-5431-2294>
 Nguyen Bich Ngoc  <https://orcid.org/0000-0002-5913-5554>
 Nagayoshi Ohashi  <https://orcid.org/0000-0003-0998-5064>
 Jonathan Rawlings  <https://orcid.org/0000-0001-5560-1303>
 Mark Rawlings  <https://orcid.org/0000-0002-6529-202X>
 Ekta Sharma  <https://orcid.org/0000-0002-4541-0607>
 Yoshito Shimajiri  <https://orcid.org/0000-0001-9368-3143>
 Xindi Tang  <https://orcid.org/0000-0002-4154-4309>
 Hoang Duc Thuong  <https://orcid.org/0000-0002-3437-5228>
 Kohji Tomisaka  <https://orcid.org/0000-0003-2726-0892>
 Le Ngoc Tram  <https://orcid.org/0000-0002-6488-8227>
 Anthony Whitworth  <https://orcid.org/0000-0002-1178-5486>
 Jinjin Xie  <https://orcid.org/0000-0002-2738-146X>
 Hyunju Yoo  <https://orcid.org/0000-0002-8578-1728>
 Hyeong-Sik Yun  <https://orcid.org/0000-0001-6842-1555>

Yapeng Zhang  <https://orcid.org/0000-0002-5102-2096>
 Jianjun Zhou  <https://orcid.org/0000-0003-0356-818X>
 Ilse de Looze  <https://orcid.org/0000-0001-9419-6355>
 Sam Falle  <https://orcid.org/0000-0002-9829-0426>
 Jean-François Robitaille  <https://orcid.org/0000-0001-5079-8573>

References

- Ajeddig, H., Adam, R., Ade, P., et al. 2022, in European Physical Journal Web of Conf., 257, ed. M. De Petris, A. Ferragamo, & F. Mayet, **00002**
- André, P., Di Francesco, J., Ward-Thompson, D., et al. 2014, in Protostars and Planets VI, ed. H. Beuther et al. (Tucson, AZ: Univ. of Arizona Press), **27**
- Arzoumanian, D., Furuya, R. S., Hasegawa, T., et al. 2021, **A&A**, **647**, **A78**
- Bailer-Jones, C. A. L., Rybizki, J., Fouesneau, M., Demleitner, M., & Andrae, R. 2021, **AJ**, **161**, **147**
- Bally, J. 2008, in Handbook of Star Forming Regions, Volume I: The Northern Sky ASP Monograph Publications, ed. B. Reipurth Vol. 4 (San Francisco, CA: ASP), **459**
- Bastien, P. 2020, in Stellar Magnetism: A Workshop in Honour of the Career and Contributions of John D. Landstreet, Proc. of the Polish Astronomical Society, 11, ed. G. Wade et al., **117**
- Chandrasekhar, S., & Fermi, E. 1953, **ApJ**, **118**, **113**
- Chen, C.-Y., Li, Z.-Y., Mazzei, R. R., et al. 2022, **MNRAS**, **514**, **1575**
- Chini, R., Reipurth, B., Ward-Thompson, D., et al. 1997, **ApJL**, **474**, **L135**
- Chuss, D. T., Andersson, B. G., Bally, J., et al. 2019, **ApJ**, **872**, **187**
- Cortés, P. C., Le Gouellec, V. J. M., Hull, C. L. H., et al. 2021, **ApJ**, **907**, **94**
- Cox, N. L. J., Arzoumanian, D., André, P., et al. 2016, **A&A**, **590**, **A110**
- Crutcher, R. M. 2012, **ARA&A**, **50**, **29**
- Currie, M. J., & Berry, D. S. 2014, KAPPA: Kernel Applications Package, Astrophysics Source Code Library, ascl:**1403.022**
- Currie, M. J., Berry, D. S., & Jenness, T. 2014, in ASP Conf. Ser. 485, Astronomical Data Analysis Software and Systems XXIII, 391, ed. N. Manset & P. Forshay (San Francisco, CA: ASP)
- Davis, L. 1951, **Physical Review**, **81**, **890**
- Dempsey, J. T., Friberg, P., Jenness, T., et al. 2013, **MNRAS**, **430**, **2534**
- Friberg, P., Bastien, P., Berry, D., et al. 2016, **Proc. SPIE**, **9914**, **991403**
- Friesen, R. K., Pineda, J. E., co-PIs, et al. 2017, **ApJ**, **843**, **63**
- Furlan, E., Fischer, W. J., Ali, B., et al. 2016, **ApJS**, **224**, **5**
- Gaia Collaboration, Brown, A. G. A., Vallenari, A., et al. 2021, **A&A**, **649**, **A1**
- Girichidis, P. 2021, **MNRAS**, **507**, **5641**
- Großschedl, J. E., Alves, J., Meingast, S., et al. 2018, **A&A**, **619**, **A106**
- Großschedl, J. E., Alves, J., Teixeira, P. S., et al. 2019, **A&A**, **622**, **A149**
- Guerra, J. A., Chuss, D. T., Dowell, C. D., et al. 2021, **ApJ**, **908**, **98**
- Hacar, A., Clark, S. E., Heitsch, F., et al. 2023, in ASP Conf. Ser. 534, Protostars and Planets VII, ed. S. Inutsuka et al. (San Francisco, CA: ASP)
- Hacar, A., Tafalla, M., Forbrich, J., et al. 2018, **A&A**, **610**, **A77**
- Hennebelle, P., & Inutsuka, S. 2019, **FrASS**, **6**, **5**
- Hildebrand, R. H., Kirby, L., Dotson, J. L., Houde, M., & Vaillancourt, J. E. 2009, **ApJ**, **696**, **567**
- Holland, W. S., Bintley, D., Chapin, E. L., et al. 2013, **MNRAS**, **430**, **2513**
- Houde, M., Dowell, C. D., Hildebrand, R. H., et al. 2004, **ApJ**, **604**, **717**
- Houde, M., Vaillancourt, J. E., Hildebrand, R. H., Chitsazadeh, S., & Kirby, L. 2009, **ApJ**, **706**, **1504**
- Hull, C. L. H., Plambeck, R. L., Kwon, W., et al. 2014, **ApJS**, **213**, **13**
- Hwang, J., Kim, J., Pattle, K., et al. 2021, **ApJ**, **913**, **85**
- Jenness, T., Chapin, E. L., Berry, D. S., et al. 2013, SMURF: Submillimeter User Reduction Facility, Astrophysics Source Code Library, ascl:**1310.007**
- Johnstone, D., & Bally, J. 1999, **ApJL**, **510**, **L49**
- Koch, E. W., & Rosolowsky, E. W. 2015, **MNRAS**, **452**, **3435**
- Lada, C. J., Muench, A. A., Haisch, K. E. J., et al. 2000, **AJ**, **120**, **3162**
- Lazarian, A. 2007, **JQSRT**, **106**, **225**
- Li, D., Tang, X., Henkel, C., et al. 2020, **ApJ**, **901**, **62**
- Li, H.-B. 2021, **Galax**, **9**, **41**
- Li, P. S., Lopez-Rodríguez, E., Soam, A., & Klein, R. I. 2022, **MNRAS**, **514**, **3024**
- Liu, J., Qiu, K., & Zhang, Q. 2022a, **ApJ**, **925**, **30**
- Liu, J., Zhang, Q., Commerçon, B., et al. 2021, **ApJ**, **919**, **79**
- Liu, J., Zhang, Q., & Qiu, K. 2022b, **FrASS**, **9**, **943556**
- Liu, Y., Takahashi, S., Machida, M., et al. 2024, **ApJ**, **963**, **104**
- Lombardi, M., Bouy, H., Alves, J., & Lada, C. J. 2014, **A&A**, **566**, **A45**
- Mac Low, M.-M., & Klessen, R. S. 2004, **RvMP**, **76**, **125**

- Mairs, S., Dempsey, J. T., Bell, G. S., et al. 2021, [AJ](#), **162**, 191
- Matthews, B. C., Lai, S.-P., Crutcher, R. M., & Wilson, C. D. 2005, [ApJ](#), **626**, 959
- Matthews, B. C., McPhee, C. A., Fissel, L. M., & Curran, R. L. 2009, [ApJS](#), **182**, 143
- Matthews, B. C., Wilson, C. D., & Fiege, J. D. 2001, [ApJ](#), **562**, 400
- McKee, C. F., & Ostriker, E. C. 2007, [ARA&A](#), **45**, 565
- Megeath, S. T., Gutermuth, R., Muzerolle, J., et al. 2012, [AJ](#), **144**, 192
- Mouschovias, T. C., Tassis, K., & Kunz, M. W. 2006, [ApJ](#), **646**, 1043
- Ostriker, E. C., Stone, J. M., & Gammie, C. F. 2001, [ApJ](#), **546**, 980
- Otter, J., Ginsburg, A., Ballering, N. P., et al. 2021, [ApJ](#), **923**, 221
- Padoan, P., Goodman, A., Draine, B. T., et al. 2001, [ApJ](#), **559**, 1005
- Pattle, K., Ward-Thompson, D., Berry, D., et al. 2017, [ApJ](#), **846**, 122
- Pillai, T. G. S., Clemens, D. P., Reissl, S., et al. 2020, [NatAs](#), **4**, 1195
- Pineda, J. E., Arzoumanian, D., Andre, P., et al. 2023, in ASP Conf. Ser. 534, Protostars and Planets VII, ed. S. Inutsuka et al. (San Francisco, CA: ASP), 233
- Planck Collaboration, Ade, P. A. R., Aghanim, N., et al. 2015, [A&A](#), **576**, A104
- Plaszczynski, S., Montier, L., Levrier, F., & Tristram, M. 2014, [MNRAS](#), **439**, 4048
- Poidevin, F., Bastien, P., & Jones, T. J. 2011, [ApJ](#), **741**, 112
- Poidevin, F., Bastien, P., & Matthews, B. C. 2010, [ApJ](#), **716**, 893
- Poidevin, F., Falceta-Gonçalves, D., Kowal, G., de Gouveia Dal Pino, E., & Mário Magalhães, A. 2013, [ApJ](#), **777**, 112
- Qiu, K., Zhang, Q., Menten, K. M., Liu, H. B., & Tang, Y.-W. 2013, [ApJ](#), **779**, 182
- Rezaei, S., Bailer-Jones, C. A. L., Soler, J. D., & Zari, E. 2020, [A&A](#), **643**, A151
- Schleuning, D. A. 1998, [ApJ](#), **493**, 811
- Schuller, F., André, P., Shimajiri, Y., et al. 2021, [A&A](#), **651**, A36
- Takahashi, S., Machida, M. N., Tomisaka, K., et al. 2019, [ApJ](#), **872**, 70
- Tang, Y.-W., Koch, P. M., Peretto, N., et al. 2019, [ApJ](#), **878**, 10
- Vallée, J. P., & Fiege, J. D. 2007, [AJ](#), **133**, 1012
- Ward-Thompson, D., Pattle, K., Bastien, P., et al. 2017, [ApJ](#), **842**, 66
- Zhang, C., Ren, Z., Wu, J., et al. 2020, [MNRAS](#), **497**, 793
- Zhang, Y., Guo, Z., Wang, H. H., & Li, H. 2019, [ApJ](#), **871**, 98
- Zielinski, N., & Wolf, S. 2022, [A&A](#), **659**, A22